Journal of Materials Chemistry A

ROYAL SOCIETY OF CHEMISTRY

PAPER

View Article Online
View Journal | View Issue

Cite this: J. Mater. Chem. A, 2024, 12, 19958

Wrinkled Ir-MnO_x nanospheres as pH-universal electrocatalysts for oxygen evolution reaction†

Li Quan,[a] Yirong Cao,[a] Jinlong Liu, *[b] Bao Yu Xia, [a] Xin Zhao*[c] and Bo You *[a]

The oxygen evolution reaction (OER) is an essential anode reaction paired with various energy conversion processes including hydrogen evolution, CO_2 reduction and nitrate reduction under diverse pH conditions, and its sluggish kinetics limits the overall energy efficiencies of those processes due to the lack of highly efficient OER electrocatalysts. Herein, we report wrinkled Ir-doped MnO_x (Ir-MnO_x) nanospheres as advanced OER electrocatalysts over a wide pH range (0–14). Benefiting from the wrinkled nanospherical morphology with a large specific area and optimal electronic structure, the resulting Ir-MnO_x shows low overpotentials of only 270, 295, and 360 mV at 10 mA cm^{-2} under acidic, alkaline and neutral conditions, respectively. Specifically, a high Ir mass activity of 1335.7 A g_{Ir}^{-1} at 1.5 V *vs.* RHE under acidic conditions can be achieved. Systematic experiments and *operando* spectroscopy characterization as well as density functional theory (DFT) calculations reveal that integrating Ir into MnO_x leads to a modulated electronic structure for optimal intermediates adsorption, and their synergy prevents the migration/aggregation of Ir species and the peroxidation of MnO_x substrates, jointly beneficial to improve the OER activity and stability.

Received 26th April 2024
Accepted 4th June 2024

DOI: 10.1039/d4ta02888k

rsc.li/materials-a

Introduction

Clean and renewable energy sources have garnered much attention due to the depletion of non-renewable fossil fuels and the associated environmental challenges.[1–4] Electrochemical processes powered by renewable electricity can convert raw feedstocks (*e.g.*, water, CO_2 and nitrate) into value-added fuels and chemicals (*e.g.*, H_2, oxygenates/hydrocarbons, and ammonia), providing a sustainable solution to alleviate the above energy and environmental issues, as well as the intermittency of renewable energy sources.[5–10] These cathodic electroreduction processes usually occur at various pH conditions and typically couple with anodic oxygen evolution reaction (OER),[11–13] such that the performance of the anode side is decisive to the overall energy efficiency. However, the OER is kinetically sluggish which involves four-electron/proton transfer, necessitating advanced electrocatalysts to reduce the reaction energy barriers for improved efficiency.[14–16] Because of diverse electrolytes with different pHs used for water splitting, CO_2 reduction and nitrate reduction, an ideal OER electrocatalyst should feature high activity and stability over a wide pH range.[17] To date, many nonprecious electrocatalysts have been proven to exhibit excellent OER performance in alkaline electrolytes.[18–21] However, most of these electrocatalysts are chemically unstable and cannot survive in harsh acidic electrolytes, leading to inferior durability.[22–24] Furthermore, under neutral conditions, the highly hydrogen-bonded interfacial water is difficult to be activated and the relatively low ionic strength limits interfacial proton/electron transfer, rendering

Bo You

Bo You received his PhD degree in 2014 under the supervision of Prof. Zhaoxiang Deng at University of Science and Technology of China (USTC). He then joined Prof. Yujie Sun's group at Utah State University from 2014 to 2016, Prof. Hong Li's group at Nanyang Technological University from 2016 to 2017, and Prof. Shi Zhang Qiao's group at The University of Adelaide from 2017 to 2019 as a postdoctoral researcher. Currently, he is a full professor at Huazhong University of Science and Technology (HUST). His research focuses on integration-designed electroactivation (IDEA) for advanced renewable energy.

[a]Key Laboratory of Material Chemistry for Energy Conversion and Storage Ministry of Education, Hubei Key Laboratory of Material Chemistry and Service Failure, School of Chemistry and Chemical Engineering, Huazhong University of Science and Technology, Wuhan, Hubei 430074, China. E-mail: youbo@hust.edu.cn

[b]College of Chemistry and Chemical Engineering, Central South University, Changsha, Hunan 410083, China. E-mail: liujinlong@csu.edu.cn

[c]Hubei Engineering Research Center of Radio Frequency Microwave Technology and Application, School of Science, Wuhan University of Technology, Wuhan, Hubei 430070, China. E-mail: xzhao@whut.edu.cn

† Electronic supplementary information (ESI) available. See DOI: https://doi.org/10.1039/d4ta02888k

the activity of the underlying electrocatalysts mediocre.[25–27] Therefore, rational design and synthesis of cost-effective and highly active OER electrocatalysts under all-pH conditions is urgently needed.

Iridium (Ir)-based materials are considered state-of-the-art OER electrocatalysts owing to their relatively high catalytic activity and decent stability under harsh conditions.[17,28] However, the limited reserves and low mass activity limit their large-scale applications.[29,30] It is thus vital to reduce the Ir dosage in electrocatalysts and/or improve their intrinsic activities. Efforts have been made to minimize Ir loading, among which integrating Ir species with suitable supports has been recognized as a reliable approach.[31,32] Moreover, the interaction between doped Ir species and substrates can not only tune the electronic structure and thus intrinsic catalytic properties of the electrocatalysts, but also improve the dispersion of Ir sites to alleviate the possible aggregation during long-term operation for boosted specific mass activity.[33,34] Specifically, manganese-based oxides are commonly used as supporting materials to construct OER electrocatalysts due to their natural abundance, affordable cost, decent activity and robust durability.[35,36] Successful attempts have been made using manganese oxides to support Ir species featuring enhanced OER performance in a narrow pH range.[29,37–40] These electrocatalysts, however, still suffer from high Ir usage and poor performance, especially in neutral or acidic media.[6,41,42] It is still challenging to develop advanced manganese oxide-supported Ir-based OER electrocatalysts in a wide pH range.

Herein, we have synthesized wrinkled Ir-doped manganese oxide (Ir-MnO_x) nanospheres as pH-universal OER electrocatalysts *via* a facile solvothermal and annealing of Ir-doped Mn-MIL-100 metal–organic frameworks. The unique morphology of wrinkled nanospheres and the abundance of porosity inherited from Mn-MIL-100 facilitate mass transfer and access of active sites. Introduction of Ir species in MnO_x supports prevents their migration and agglomeration, and meanwhile, their synergistic effect results in a regulated electronic structure and thereby optimal adsorption of intermediates during the OER, as revealed by our combined experiments, *operando* spectroscopy characterization and theoretical calculations. Consequently, the resulting Ir-MnO_x exhibits superior OER activity and stability, outperforming the state-of-the-art IrO_2 benchmark electrocatalyst in the whole pH range (0–14). For instance, under acidic conditions, the resulting Ir-MnO_x exhibits a low overpotential of only 270 mV at 10 mA cm^{-2}, and high Ir mass activity of 1335.7 A g_{Ir}^{-1} which is 150 times higher than that of commercial IrO_2 (8.9 A g_{Ir}^{-1}) at 1.5 V *vs.* RHE. In addition, Ir-MnO_x also shows excellent activity under alkaline and neutral conditions, with respective overpotentials of only 295 and 360 mV to reach 10 mA cm^{-2} as well as robust stability. This work may provide a plausible strategy for the design and synthesis of highly active, low-cost, and reliable pH-universal OER electrocatalysts.

Results and discussion

The synthetic process of Ir-MnO_x is illustrated in Fig. 1a (see the ESI† for details). The Ir-doped Mn-MIL-100 precursor was first synthesized by a one-pot solvothermal route in the presence of $Mn(NO_3)_2$, Na_3IrCl_6, and organic ligand of 1,3,5-benzenetricarboxylicacid, and then subjected to high-temperature annealing at 450 °C under air conditions. As shown in Fig. 1b, the scanning electron microscopy (SEM) image of the Ir-doped Mn-MIL-100 precursor reveals a nanosphere-like morphology with a smooth surface, different from the octahedral structure of Mn-MIL-100 without the Na_3IrCl_6 precursor (Fig. S1†). After annealing in air, the Ir-doped Mn-MIL-100 precursor was converted to the target Ir-MnO_x, and the nanosphere-like structure was maintained with reduced particle size as depicted in the SEM image (Fig. 1c). The TEM image of Ir-MnO_x reveals a clear structure featuring a hollow interior and wrinkled surface (Fig. 1d), due to the faster outward diffusion of metal ions relative to the inward diffusion of O_2 gas during annealing.[43] The plentiful wrinkles of Ir-MnO_x contribute to increased specific surface area and facilitated accessibility of active sites for improved mass transfer and electrocatalytic activity.[44,45] The more detailed nanostructure of Ir-MnO_x was further investigated by high-resolution transmission electron microscopy (HRTEM). As displayed in Fig. 1e, the HRTEM image of Ir-MnO_x demonstrates obvious lattice spacings of 0.192, 0.249, 0.277, and 0.272 nm, assignable to the (200) facet of Ir (PDF#06-0598), (211) and (103) facets of Mn_3O_4 (PDF#24-0734), and (222) facet of Mn_2O_3 (PDF#41-1442), respectively. This result implies the coexistence of Mn_2O_3 and Mn_3O_4 in Ir-MnO_x and the successful incorporation of metallic Ir which was further evidenced by the Ir(200) diffraction ring in the selected area electron diffraction (SAED) pattern (Fig. 1f). Elemental mapping images of Ir-MnO_x (Fig. 1g) indicate that Ir, Mn, and O are uniformly dispersed throughout the whole nanosphere, further confirming the incorporation of Ir into MnO_x. In addition, inductively coupled plasma-atomic emission spectrometry (ICP-AES) verifies that the Ir content in Ir-MnO_x is only 6.1 wt%.

The phase and crystal structure of Ir-MnO_x were investigated by X-ray diffraction (XRD). As shown in Fig. 2a, the diffraction peaks at 23.1°, 32.9° and 55.2° can be assigned to the (211), (222) and (440) facets of Mn_2O_3, respectively, whereas the diffraction peaks at 18°, 28.9°, 32.3°, 36.1°, and 59.8° correspond to the (101), (112), (103), (211), and (224) facets of Mn_3O_4, respectively. Furthermore, the characteristic diffraction peaks of metallic Ir are also observed at 40.7° and 47.3°. It is worth noting that only peaks attributed to Mn_2O_3 can be observed for the control sample (denoted as Mn_2O_3) obtained by similar annealing of Mn-MIL-100 (Fig. S2†), indicative of the tuned electronic state of Mn after Ir incorporation. X-ray photoelectron spectroscopy (XPS) measurements were then conducted to analyse the chemical composition and electronic structure of Ir-MnO_x. The XPS survey spectrum evidences the presence of Ir, Mn, and O elements in Ir-MnO_x (Fig. S3†), consistent with the elemental mapping results (Fig. 1g). As depicted in Fig. 2b, the high-resolution O 1s spectrum of Ir-MnO_x can be deconvoluted into lattice oxygen (metal–O) at a binding energy of 529.8 eV (53.4%), surface adsorbed oxygen (metal–OH) at a binding energy of 531.2 eV (37.3%), and oxygen in adsorbed H_2O at a binding energy of 533.0 eV (9.3%).[46–48] Compared to the Mn_2O_3 control, Ir-MnO_x shows a decreased content of lattice oxygen

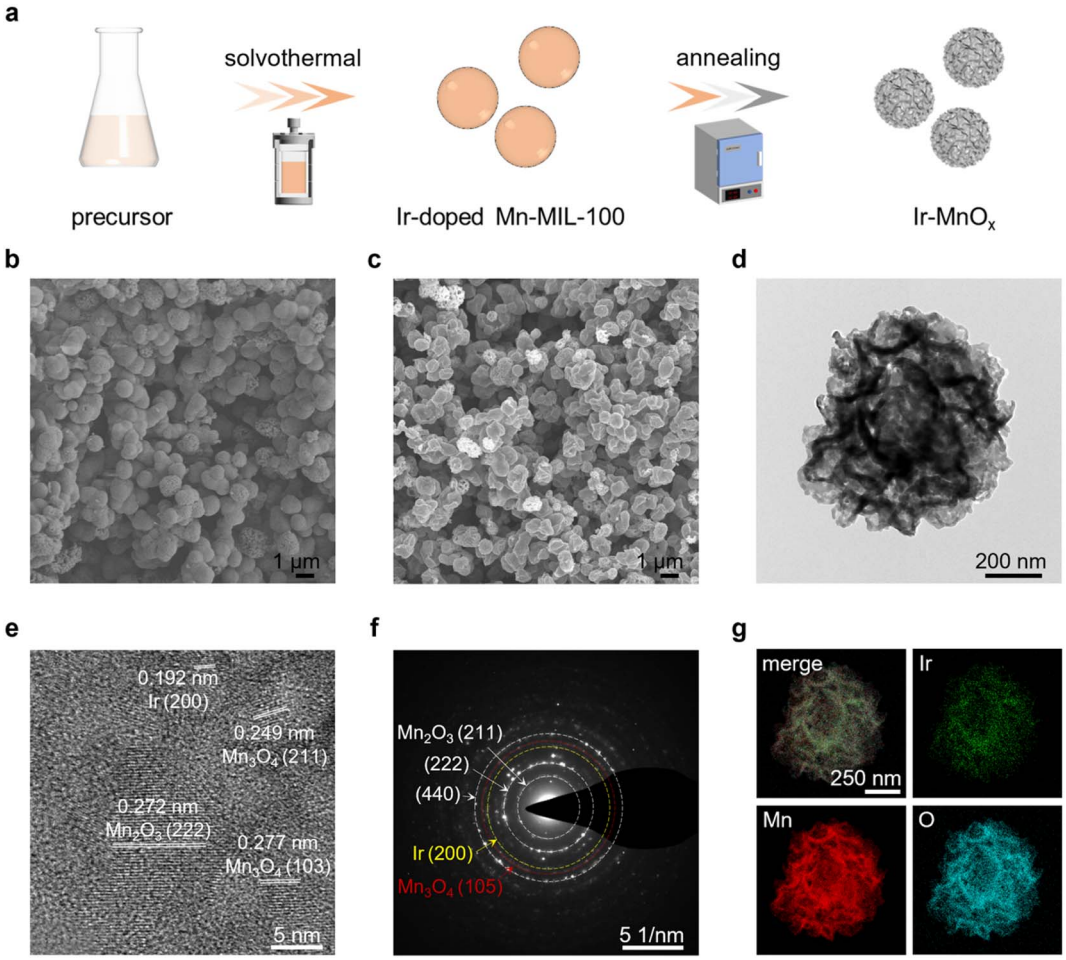

Fig. 1 (a) Schematic for the preparation of Ir-MnO$_x$. SEM images of (b) Ir-doped Mn-MIL-100 and (c) Ir-MnO$_x$. (d and e) TEM images at different magnifications and (f) SAED pattern of Ir-MnO$_x$. (g) Elemental mapping images of Ir-MnO$_x$.

and an increased content of surface adsorbed oxygen, which is beneficial for the OER following the adsorbate evolution mechanism.[12,29,49–51] In the high-resolution Mn 2p spectrum of Ir-MnO$_x$ (Fig. 2c), the binding energies of Mn 2p$_{3/2}$ peak at 641.2 and 642.4 eV and those of Mn 2p$_{1/2}$ peak at 652.0, and 653.6 eV can be assigned to Mn^{2+} and Mn^{3+}, respectively.[52–54] Besides, in the Mn 2p spectrum of Mn_2O_3, the peaks observed at 642.0 eV and 653.3 eV can be assigned to Mn^{3+}. Apparently, the peak of Mn^{2+} appears in Ir-MnO$_x$, indicating the reduced oxidation state of Mn after doping Ir and a strong interaction between them.[36] Compared with Mn_2O_3, a mixed Mn^{2+}/Mn^{3+} oxidation state exists in Ir-MnO$_x$, which can accelerate the charge transfer[55] and confer greater coordination flexibility around the Ir sites.[56,57] Besides, in the high-resolution Ir 4f XPS spectrum (Fig. 2d) of Ir-MnO$_x$, the peaks at binding energies of 61.7 and 64.6 eV can be assigned to Ir 4f$_{7/2}$ and Ir 4f$_{5/2}$ of metallic Ir.[58,59] Relative to IrO$_x$, metallic Ir may exhibit greater corrosion resistance and better conductivity,[60,61] which can reduce the OER overpotential to mitigate the peroxidation of MnO$_x$.[62] Collectively, doping Ir into MnO$_x$ modulates the electronic structure of the resulting Ir-MnO$_x$ electrocatalysts, providing the possibility to optimize the adsorption of intermediates during the OER, and the MnO$_x$ supports provide robust anchor sites for highly active Ir species to increase the durability under harsh conditions. Both synergistically enhance the OER activity and stability of the resulting Ir-MnO$_x$ electrocatalysts.

The electrocatalytic OER activities of Ir-MnO$_x$ along with Mn_2O_3 and commercial IrO_2 as controls were first analysed in strong acidic media (1 M $HClO_4$) with a three-electrode system. As illustrated in the OER polarization curves (Fig. 3a), Ir-MnO$_x$ exhibits a small overpotential of only 270 mV at a current density of 10 mA cm^{-2} (η_{10} = 270 mV), which is much lower than those of Mn_2O_3 (η_{10} = 507 mV), commercial IrO_2 (η_{10} = 326 mV) and many reported electrocatalysts (Table S1†). To confirm the current contribution from the OER rather than other possible side reactions like self-oxidation of electrocatalysts or two-electron water oxidation, the faradaic efficiency (FE) of Ir-MnO$_x$ for oxygen generation was investigated using a rotating ring disk electrode (RRDE) (Fig. S4†). The nearly 100% FE of Ir-MnO$_x$ at 1.45 V *vs.* RHE demonstrates the exclusive contribution from the OER. With increasing potential, the FE of oxygen decreases due to the massive generation of oxygen bubbles which cannot be collected at the ring electrode completely.[63,64] Furthermore, the Tafel slope of Ir-MnO$_x$ (51.5 mV dec^{-1}) is

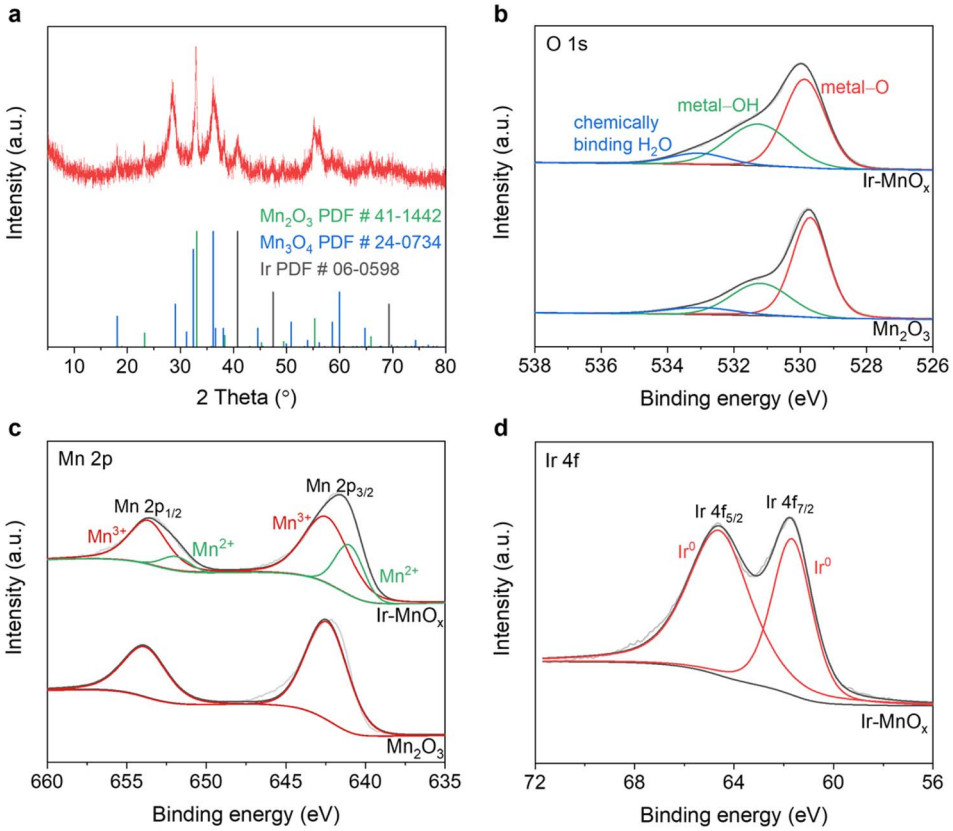

Fig. 2 (a) XRD pattern of Ir-MnO_x. (b) High-resolution O 1s XPS spectra of Ir-MnO_x and Mn_2O_3. (c) High-resolution Mn 2p XPS spectra of Ir-MnO_x and Mn_2O_3. (d) High-resolution Ir 4f XPS spectra of Ir-MnO_x.

much smaller than those of Mn_2O_3 (150.4 mV dec^{-1}) and commercial IrO_2 (77.1 mV dec^{-1}), indicating a more favourable OER kinetics (Fig. 3b). Notably, the specific mass activity of Ir-MnO_x was calculated to be 1335.7 A g_{Ir}^{-1} at 1.5 V *vs.* RHE, 150 times higher than that of commercial IrO_2 (8.9 A g_{Ir}^{-1}, Fig. 3c). Besides the specific mass activity, the turnover frequency (TOF) also offers insights into the intrinsic activity of Ir species. The calculated TOF at 1.5 V *vs.* RHE is 0.665 s^{-1} for Ir-MnO_x, more than two orders of magnitude higher than that of commercial IrO_2 (0.004 s^{-1}). The positive effect of Ir with MnO_x can also be corroborated by the electrochemical impedance spectroscopy (EIS) measurements in which Ir-MnO_x presents the smallest radius in the Nyquist plot (Fig. 3d), indicating its lowest charge transfer resistance. To assess the electrochemically active surface area (ECSA) of an electrocatalyst, the double layer capacitance (C_{dl}) is usually used as an indicator. Specifically, by conducting cyclic voltammogram (CV) measurements within the non-faradaic region at different scan rates (Fig. S5†), the calculated C_{dl} of Ir-MnO_x is 7.64 mF cm^{-2} (Fig. 3e), much higher than that of Mn_2O_3 (0.78 mF cm^{-2}) and commercial IrO_2 (3.10 mF cm^{-2}). This is attributed to the unique structure of the wrinkled nanospheres, which greatly increase the exposed surface area and active sites of the Ir-MnO_x electrocatalysts. To further get insight into the intrinsic activity, the ECSA-normalized polarization curves were obtained (Fig. 3f). It is obvious that the specific area activity at 1.6 V *vs.* RHE of Ir-MnO_x (0.11 mA cm_{ECSA}^{-2}) is higher than those of Mn_2O_3 (0.04 mA cm_{ECSA}^{-2}) and commercial IrO_2 (0.08 mA cm_{ECSA}^{-2}). These results explicitly demonstrate the superior intrinsic OER activity of Ir-MnO_x.

The durability of an OER electrocatalyst in a harsh acidic environment at high oxidation potential is another key parameter and challenging for practical application, so the stability measurements of the three electrocatalysts were evaluated in 1 M $HClO_4$ as well. Fig. 3g illustrates the chronopotentiometric responses of the three electrocatalysts at a constant current density of 10 mA cm^{-2} in an H-type water electrolyzer with the anode and cathode separated by a Nafion 117 membrane. The overpotential of commercial IrO_2 increased abruptly after only 5 h, and similarly, the Mn_2O_3 control can survive only 5 h as well. Remarkably, Ir-MnO_x can deliver a relatively stable potential at 10 mA cm^{-2} for more than 40 h with an increase of 10.3%, outperforming most reported OER electrocatalysts (Fig. 3h and Table S1†). The excellent acidic OER stability of Ir-MnO_x can be attributed to the synergistic effect between Ir and MnO_x substrates, wherein introducing highly active Ir lowers the overpotential to inhibit peroxidation of MnO_x and the effective anchoring of Ir by MnO_x alleviates their aggregation and leaching during the electrocatalytic OER process.

After stability testing, the resulting post-OER electrocatalysts were also thoroughly examined to further reveal the real active

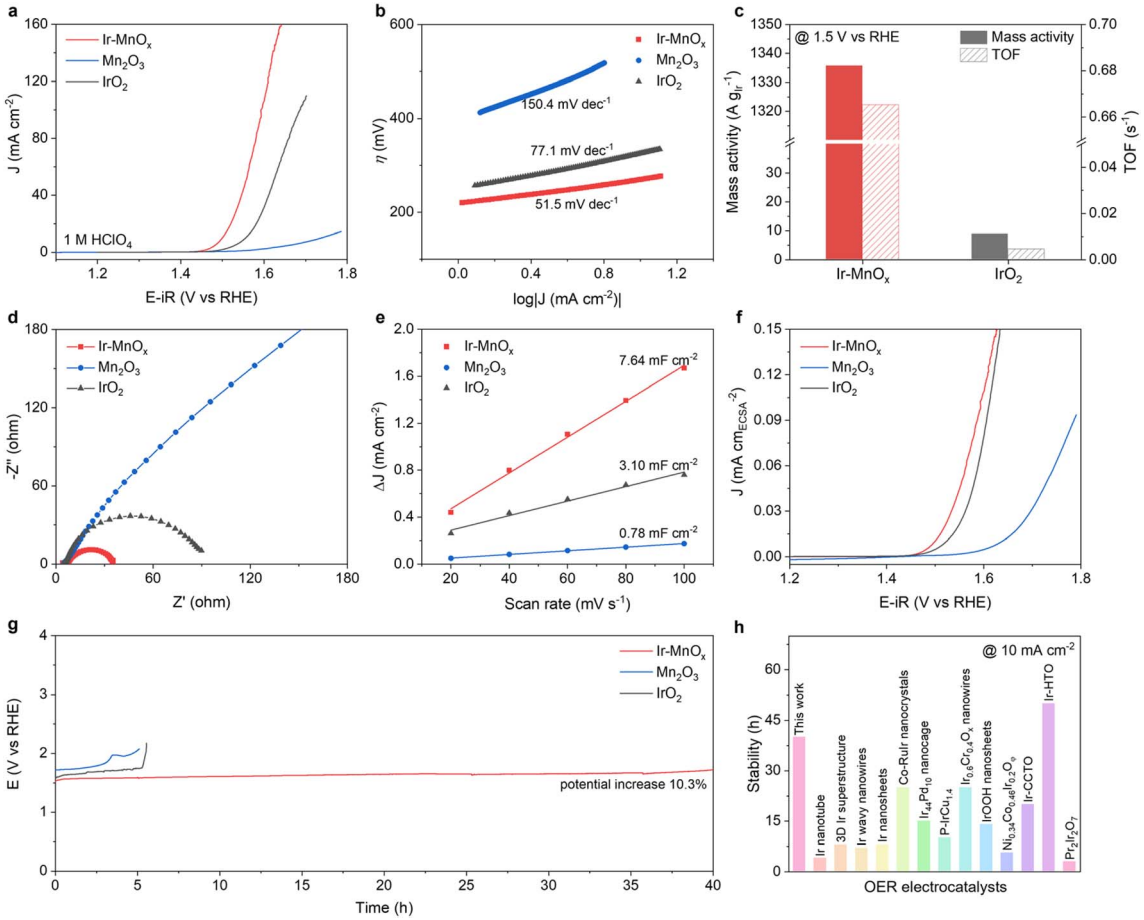

Fig. 3 Electrocatalytic OER performance of different electrocatalysts in 1 M $HClO_4$. (a) Polarization curves. (b) Tafel plots. (c) Specific mass activity and TOF based on the polarization curves and selectivity. (d) Nyquist plots. (e) C_{dl} derived from CV curves. (f) ECSA normalized polarization curves. (g) Durability tests recorded at a constant current density of 10 mA cm^{-2}. (h) Stability comparison with recently reported OER electrocatalysts.

sites. As confirmed by SEM and TEM images in Fig. S6a and b,† the wrinkled nanospherical structure of post-OER Ir-MnO_x is maintained, demonstrating the good structural stability of Ir-MnO_x. A well-defined lattice fringe with a spacing of 0.255 nm coinciding with the (101) face of IrO_2 (PDF#43-1019) can be observed from the HRTEM image of post-OER Ir-MnO_x (Fig. S6c†). Meanwhile, the corresponding SAED pattern in Fig. S6d† shows several diffraction rings corresponding to the (211) facet of Mn_3O_4 (PDF#27-0734) and (110) facet of IrO_2 (PDF#43-1019). The XRD pattern further confirms the changes of metallic Ir and mixed Mn_3O_4/Mn_2O_3 in pristine Ir-MnO_x to IrO_2 and phase-pure Mn_3O_4 after the OER (Fig. 4a), respectively. These results exactly suggest the electrochemical reconstruction of Ir-MnO_x during the OER, similar to reported OER electrocatalysts.[60,65–67] The inhibited oxidation of MnO_x supports in Ir-MnO_x may account for the robust stability, and the details of this OER-triggered reconstruction of Ir-MnO_x deserve further studies in the future.

To further explore the possible electrocatalytic OER mechanism of Ir-MnO_x, *operando* attenuated total reflection surface-enhanced Fourier-transform infrared spectroscopy (ATR-SEIRS) measurements and DFT computations were carried out. Previous studies have unveiled that switching the OER pathway from the lattice-oxygen mediated mechanism (LOM) to the adsorbate evolution mechanism (AEM) contributes to the improved stability for many acidic OER electrocatalysts, wherein the absence of lattice oxygen effectively prevents the structural collapse.[68–70] In this study, the binding of oxygen-containing intermediates (*e.g.*, *OH, *O, and *OOH) on the surface of Ir-MnO_x was investigated by *operando* ATR-SEIRS in the potential range from open-circuit potential (OCP) to 2.0 V *vs.* RHE in 1 M $HClO_4$. Along with positive scanning potentials from 1.4 to 2.0 V *vs.* RHE, Ir-MnO_x exhibits a clear peak at 1224 cm^{-1} corresponding to the O–O stretching vibration of *OOH (Fig. 4b), which is a typical intermediate in the AEM pathway.[71] Notably, the gradually increased peak intensity of *OOH over Ir-MnO_x without the emergence of new peaks indicates that Ir-MnO_x follows the AEM pathway with accelerated oxidation. By comparison, the commercial IrO_2 (Fig. 4c) shows a weak peak intensity of *OOH even at higher potentials exceeding 1.6 V *vs.* RHE, indicative of the slower OER kinetics relative to Ir-MnO_x. DFT calculations were then performed to

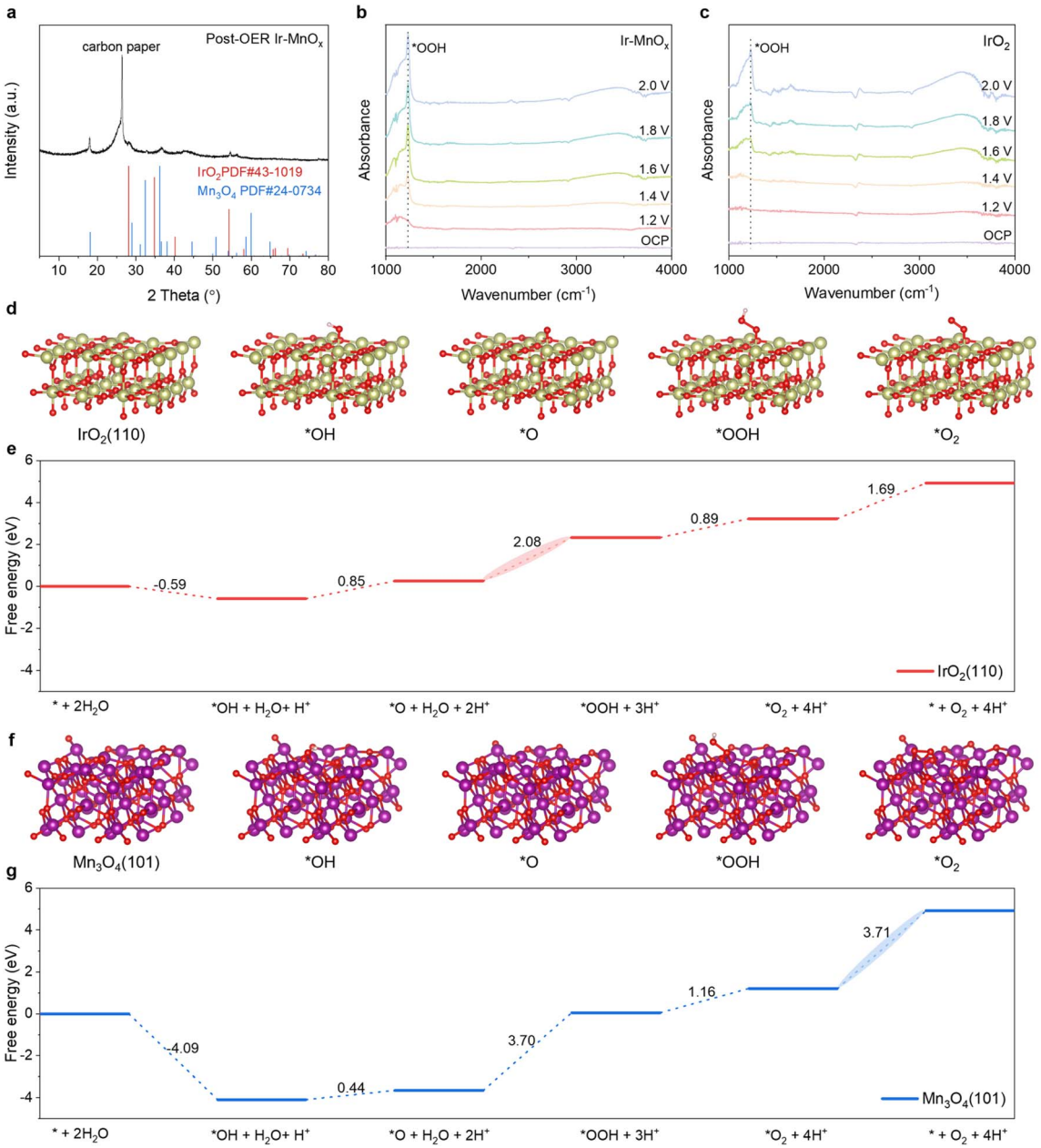

Fig. 4 (a) XRD pattern of post-OER Ir-MnO_x. *Operando* ATR-SEIRS measurements of (b) Ir-MnO_x and (c) IrO_2 at various applied potentials, and all potentials were normalized against the RHE. Structure models of reaction intermediate for the OER on (d) IrO_2(110) and (f) Mn_3O_4(101) surfaces. Gibbs free energy diagrams for the OER at 0 V *vs.* RHE on (e) IrO_2(110) and (g) Mn_3O_4(101) surfaces. The rate-limiting steps are marked with shadows.

provide an in-depth insight into the improved OER activity of Ir-MnO_x. Based on the HRTEM, SAED and XRD results of post-OER Ir-MnO_x, the most exposed lowest-energy planes of IrO_2(110) and Mn_3O_4(101) were used as models for theoretical calculations. The structure models of reaction intermediates of the OER on IrO_2(110) and Mn_3O_4(101) surfaces are shown in Fig. 4d and f. Moreover, the Gibbs free energy diagram of IrO_2(110) and Mn_3O_4(101) surfaces for the OER based on the AEM at zero electrode potential were calculated. As demonstrated in Fig. 4e and g, the rate-determining step (RDS) of IrO_2(110) is the conversion of *O to *OOH with a Gibbs free energy change (ΔG) of 2.08 eV, much lower than that of the RDS on Mn_3O_4(101) (3.71 eV). This comparison indicates that IrO_2 is the active species of the OER.[72] However, it is noticed that the ΔG values of OH^- adsorption and subsequent oxidation on the Mn_3O_4(101) surface are smaller than those on IrO_2(110), indicating a more favourable adsorption of OH^- and the subsequent oxidation to *O formation on the former.[73,74] Therefore, it is expected that incorporating IrO_2 and Mn_3O_4 in Ir-MnO_x can synergistically modulate the adsorption of OH^- and individual oxygen-containing intermediates during the OER process for enhanced electrocatalytic activity.

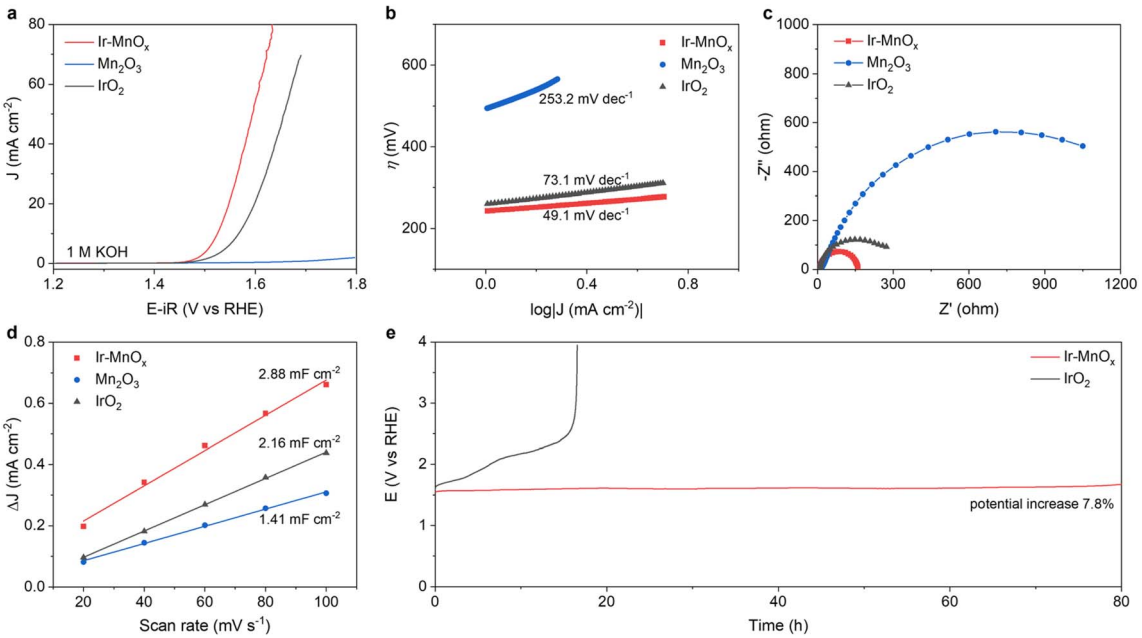

Fig. 5 Electrocatalytic OER performance of different electrocatalysts in 1 M KOH. (a) Polarization curves. (b) Tafel plots. (c) Nyquist plots. (d) C_{dl} derived from CV curves. (e) Durability tests recorded at a constant current density of 10 mA cm^{-2}.

To satisfy the requirements for versatile electrocatalytic applications in a wide pH range, the OER performance of Ir-MnO_x was also measured under alkaline (1 M KOH) and neutral (1 M PBS) conditions. In 1 M KOH, the polarization curve (Fig. 5a) of Ir-MnO_x reveals a low overpotential of 295 mV to reach a current density of 10 mA cm^{-2}, in sharp contrast to those of Mn_2O_3 (>500 mV), IrO_2 (337 mV), and many other reported catalysts (Table S2†). Furthermore, Ir-MnO_x displays an ultralow Tafel slope of 49.1 mV dec^{-1}, much lower than those of Mn_2O_3 (253.2 mV dec^{-1}) and IrO_2 (73.1 mV dec^{-1}), indicating the favourable OER kinetics of the former under alkaline conditions (Fig. 5b). The Nyquist plots (Fig. 5c) and electrochemical double-layer capacitance measurements (Fig. 5d and S7†) indicate that Ir-MnO_x possesses lower charge transfer resistance and larger ECSA relative to those of Mn_2O_3 and IrO_2, respectively. Remarkably, the unique morphology and modified

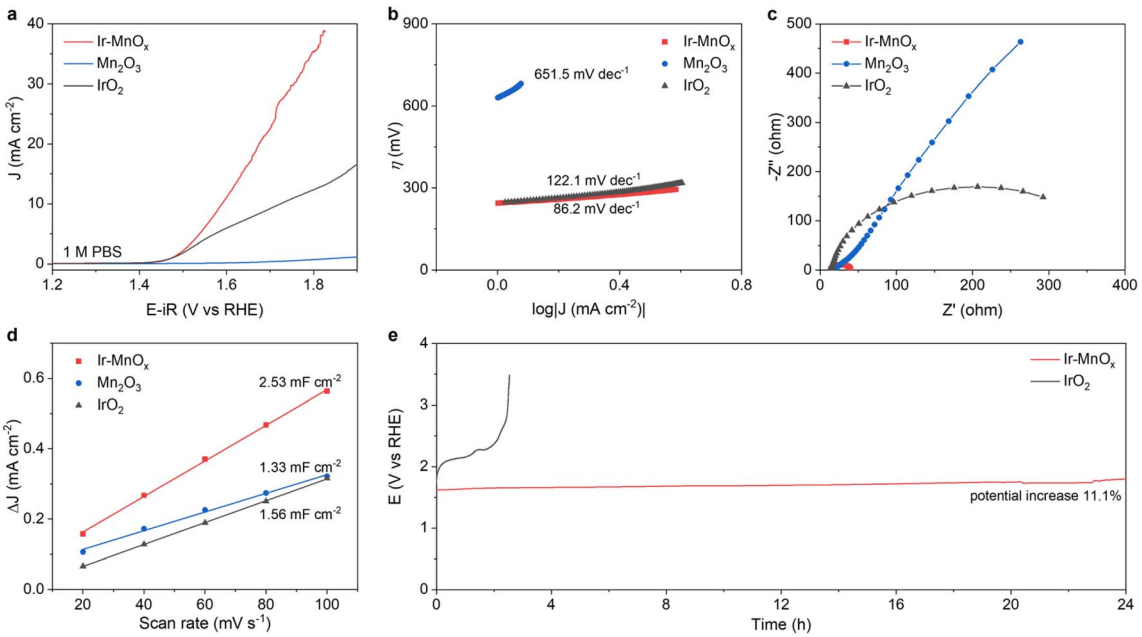

Fig. 6 Electrocatalytic OER performance of different electrocatalysts in 1 M PBS. (a) Polarization curves. (b) Tafel plots. (c) Nyquist plots. (d) C_{dl} derived from CV curves. (e) Durability tests recorded at a constant current density of 10 mA cm^{-2}.

electronic structure endow Ir-MnO_x with outstanding durability for 80 h electrocatalysis at 10 mA cm^{-2} in 1 M KOH, with a potential increase of 7.8%. By contrast, the commercial IrO_2 benchmark shows apparent deactivation within 15 h (Fig. 5e).

Finally, the OER performance of our Ir-MnO_x under neutral conditions (1 M PBS) was studied as well. Compared to acidic and alkaline electrolytes, the strong hydrogen-bonding network and slow proton transfer under neutral conditions usually lead to the difficult activation of water molecules and thus poor OER activity of the underlying electrocatalysts.[25,75] While benefitting from the structure advantages of Ir-MnO_x, high OER performance can be still achieved in 1 M PBS. As illustrated in Fig. 6a, the overpotential of Ir-MnO_x is only 360 mV at 10 mA cm^{-2}, significantly lower than those of Mn_2O_3 (>500 mV), IrO_2 (494 mV), and many other reported catalysts (Table S3†). The Tafel slope of Ir-MnO_x is 86.2 mV dec^{-1} as shown in Fig. 6b, which is remarkably lower than those of Mn_2O_3 (651.5 mV dec^{-1}) and commercial IrO_2 (122.1 mV dec^{-1}), revealing faster OER kinetics of Ir-MnO_x in neutral electrolyte. Similarly, the Nyquist plot of Ir-MnO_x (Fig. 6c) exhibits lower charge transfer resistance compared to those of Mn_2O_3 and IrO_2, indicative of the faster OER process, which is in line with the Tafel analysis. Additionally, the C_{dl} of Ir-MnO_x (2.53 mF cm^{-2}) is larger than those of Mn_2O_3 (1.33 mF cm^{-2}) and IrO_2 (1.56 mF cm^{-2}) as depicted in Fig. 6d and S8†, demonstrating the larger ECSA of Ir-MnO_x. To assess the stability of the catalysts, chronopotentiometry measurements were performed on Ir-MnO_x and IrO_2 (Fig. 6e). Ir-MnO_x exhibits a slight potential increase (11.1%) at a constant current density of 10 mA cm^{-2} after 24 h. In contrast, a rapid increase in potential for commercial IrO_2 can be observed after only 3 h.

Based on the above electrochemical experiments, *operando* spectroscopy characterization and DFT calculations, we expect that the excellent electrocatalytic OER performance of Ir-MnO_x over a broad pH range can be attributed to the unique properties: (1) the morphology of wrinkled nanospheres with abundant porosity which provides a large specific surface area for high accessibility of active sites and facilitated mass transfer, (2) the integration of Ir with MnO_x substrates which optimizes the electronic structure of the resulting Ir-MnO_x and thus critical intermediate adsorption during the OER process, and (3) the synergistic effect between Ir and MnO_x due to which the MnO_x supports with excellent acid resistance stabilize the anchored Ir species to prevent their aggregation, and the Ir species significantly reduces the overpotentials during the OER to inhibit the peroxidation of MnO_x.

Conclusions

In summary, we have demonstrated a facile metal–organic framework-directed strategy to synthesize wrinkled Ir-doped manganese oxide (Ir-MnO_x) nanospheres as highly active and stable OER electrocatalysts over a broad pH range (0–14). The wrinkled sphere-like morphology and plentiful porosity facilitate mass transfer and access of active sites. The coupling configuration of Ir with MnO_x prevents the agglomeration of active Ir species, and synergistically results in a regulated electronic structure for optimal adsorption of critical intermediates, as confirmed by our combined experiments, *operando* spectroscopy characterization and DFT calculations. With these tailored architectures, the resulting Ir-MnO_x exhibits prominent OER activity and stability in acidic (1 M $HClO_4$), alkaline (1 M KOH), and neutral (1 M PBS) solutions with respective overpotentials of 270, 295, and 360 mV at 10 mA cm^{-2}, much smaller than those of commercial IrO_2 benchmark. Particularly, the specific mass activity and TOF of Ir-MnO_x in 1 M $HClO_4$ are up to 1335.7 A g_{Ir}^{-1} and 0.665 s^{-1} at 1.5 V *vs.* RHE, both of which are two orders of magnitude higher than those of commercial IrO_2 benchmark (8.9 A g_{Ir}^{-1} and 0.004 s^{-1}). This work provides a new guideline for the development of high performance, cost-effective and pH-universal OER electrocatalysts.

Author contributions

Li Quan: investigation, data curation, formal analysis, writing – original draft. Yirong Cao: formal analysis. Jinlong Liu: DFT calculations and analysis. Bao Yu Xia: writing – review & editing. Xin Zhao: writing – review & editing. Bo You: supervision, conceptualization, formal analysis, writing – review & editing.

Conflicts of interest

The authors declare no conflict of interest.

Acknowledgements

This work was financially supported by The National Key Research and Development Program of China (2021YFA1600800), the National Natural Science Foundation of China (12304488, 22075092 and 52103354), and The Innovation and Talent Recruitment Base of New Energy Chemistry and Device (B21003). Also, we are grateful to the High-Performance Computing Centre of Central South University for assistance with the computations, and the Analytical and Testing Center of Huazhong University of Science and Technology for several physiochemical characterizations.

Notes and references

1 S. Chu and A. Majumdar, *Nature*, 2012, **488**, 294–303.
2 M. S. Dresselhaus and I. L. Thomas, *Nature*, 2001, **414**, 332–337.
3 L. Quan, H. Jiang, G. Mei, Y. Sun and B. You, *Chem. Rev.*, 2024, **124**, 3694–3812.
4 H. Jiang, Y. Sun and B. You, *Acc. Chem. Res.*, 2023, **56**, 1421–1432.
5 L. C. Seitz, C. F. Dickens, K. Nishio, Y. Hikita, J. Montoya, A. Doyle, C. Kirk, A. Vojvodic, H. Y. Hwang, J. K. Norskov and T. F. Jaramillo, *Science*, 2016, **353**, 1011–1014.
6 Q. Shi, C. Zhu, D. Du and Y. Lin, *Chem. Soc. Rev.*, 2019, **48**, 3181–3192.
7 X. Zhao, D. He, B. Y. Xia, Y. Sun and B. You, *Adv. Mater.*, 2023, **35**, 2210703.

8 L. Du, H. Xiong, H. Lu, L.-M. Yang, R.-Z. Liao, B. Y. Xia and B. You, *Exploration*, 2022, **2**, 20220024.
9 Z. Zhu, X. Zhao, B. Y. Xia and B. You, *ChemSusChem*, 2024, **17**, e202301213.
10 Z. Zhu, X. Chen, J. Liu, S. Fan and B. You, *Energy Fuels*, 2023, **37**, 18038–18045.
11 N.-T. Suen, S.-F. Hung, Q. Quan, N. Zhang, Y.-J. Xu and H. M. Chen, *Chem. Soc. Rev.*, 2017, **46**, 337–365.
12 Y. Jiao, Y. Zheng, M. Jaroniec and S. Z. Qiao, *Chem. Soc. Rev.*, 2015, **44**, 2060–2086.
13 S. M. Alia, S. Shulda, C. Ngo, S. Pylypenko and B. S. Pivovar, *ACS Catal.*, 2018, **8**, 2111–2120.
14 F.-Y. Chen, Z.-Y. Wu, Z. Adler and H. Wang, *Joule*, 2021, **5**, 1704–1731.
15 H. Ding, H. Liu, W. Chu, C. Wu and Y. Xie, *Chem. Rev.*, 2021, **121**, 13174–13212.
16 L. Quan, X. Chen, J. Liu, S. Fan, B. Y. Xia and B. You, *Adv. Funct. Mater.*, 2023, **33**, 2307643.
17 L. Zhang, H. Jang, H. Liu, M. G. Kim, D. Yang, S. Liu, X. Liu and J. Cho, *Angew. Chem., Int. Ed.*, 2021, **60**, 18821–18829.
18 X. Xia, L. Wang, N. Sui, V. L. Colvin and W. W. Yu, *Nanoscale*, 2020, **12**, 12249–12262.
19 N. Han, P. Liu, J. Jiang, L. Ai, Z. Shao and S. Liu, *J. Mater. Chem. A*, 2018, **6**, 19912–19933.
20 Q. Hu, G. Li, Z. Han, Z. Wang, X. Huang, H. Yang, Q. Zhang, J. Liu and C. He, *J. Mater. Chem. A*, 2019, **7**, 14380–14390.
21 S. Li, E. Li, X. An, X. Hao, Z. Jiang and G. Guan, *Nanoscale*, 2021, **13**, 12788–12817.
22 Y. Lin, Y. Dong, X. Wang and L. Chen, *Adv. Mater.*, 2023, **35**, 2210565.
23 C. Rong, K. Dastafkan, Y. Wang and C. Zhao, *Adv. Mater.*, 2023, **35**, 2211884.
24 Q. Wang, Y. Cheng, H. B. Tao, Y. Liu, X. Ma, D.-S. Li, H. B. Yang and B. Liu, *Angew. Chem., Int. Ed.*, 2023, **62**, e202216645.
25 Y. Hao, Y. Kang, S. Wang, Z. Chen, C. Lei, X. Cao, L. Chen, Y. Li, Z. Liu and M. Gong, *Angew. Chem., Int. Ed.*, 2023, **62**, e202303200.
26 K. Zhao, Y. Tao, L. Fu, C. Li and B. Xu, *Angew. Chem., Int. Ed.*, 2023, **62**, e202308335.
27 S. Zhao, Y. Wang, Y. Hao, L. Yin, C.-H. Kuo, H.-Y. Chen, L. Li and S. Peng, *Adv. Mater.*, 2024, **36**, 2308925.
28 J. Feng, F. Lv, W. Zhang, P. Li, K. Wang, C. Yang, B. Wang, Y. Yang, J. Zhou, F. Lin, G.-C. Wang and S. Guo, *Adv. Mater.*, 2017, **29**, 1703798.
29 W. Zhao, F. Xu, L. Liu, M. Liu and B. Weng, *Adv. Mater.*, 2023, **35**, 2308060.
30 Q. Dang, H. Lin, Z. Fan, L. Ma, Q. Shao, Y. Ji, F. Zheng, S. Geng, S.-Z. Yang, N. Kong, W. Zhu, Y. Li, F. Liao, X. Huang and M. Shao, *Nat. Commun.*, 2021, **12**, 6007.
31 H. Su, W. Zhou, W. Zhou, Y. Li, L. Zheng, H. Zhang, M. Liu, X. Zhang, X. Sun, Y. Xu, F. Hu, J. Zhang, T. Hu, Q. Liu and S. Wei, *Nat. Commun.*, 2021, **12**, 6118.
32 Z. Lei, W. Cai, Y. Rao, K. Wang, Y. Jiang, Y. Liu, X. Jin, J. Li, Z. Lv, S. Jiao, W. Zhang, P. Yan, S. Zhang and R. Cao, *Nat. Commun.*, 2022, **13**, 24.
33 C. Cai, M. Wang, S. Han, Q. Wang, Q. Zhang, Y. Zhu, X. Yang, D. Wu, X. Zu, G. E. Sterbinsky, Z. Feng and M. Gu, *ACS Catal.*, 2021, **11**, 123–130.
34 X. Zheng, M. Qin, S. Ma, Y. Chen, H. Ning, R. Yang, S. Mao and Y. Wang, *Adv. Sci.*, 2022, **9**, 2104636.
35 Z. Wang, W. Gao, Q. Xu, X. Ren, S. Xu, S. Zhu, X. Niu, X. Li, R. Zhao, Y. Han, G. Li and Q. Wang, *ChemElectroChem*, 2021, **8**, 418–424.
36 Y. Weng, K. Wang, S. Li, Y. Wang, L. Lei, L. Zhuang and Z. Xu, *Adv. Sci.*, 2023, **10**, 2205920.
37 Z. Shi, Y. Wang, J. Li, X. Wang, Y. Wang, Y. Li, W. Xu, Z. Jiang, C. Liu, W. Xing and J. Ge, *Joule*, 2021, **5**, 2164–2176.
38 H. Su, C. Yang, M. Liu, X. Zhang, W. Zhou, Y. Zhang, K. Zheng, S. Lian and Q. Liu, *Nat. Commun.*, 2024, **15**, 95.
39 S. Park, T. Jang, S. Choi, Y. H. Lee, K. H. Cho, M. Y. Lee, H. Seo, H. K. Lim, Y. Kim, J. Ryu, S. W. Im, M. G. Kim, J.-S. Park, M. Kim, K. Jin, S. H. Kim, G.-S. Park, H. Kim and K. T. Nam, *J. Am. Chem. Soc.*, 2023, **145**, 26632–26644.
40 K. Hua, X. Li, Z. Rui, X. Duan, Y. Wu, D. Yang, J. Li and J. Liu, *ACS Catal.*, 2024, **14**, 3712–3724.
41 Z. Lin, T. Wang and Q. Li, *Ind. Chem. Mater.*, 2023, **1**, 299–311.
42 N. T. T. Thao, J. U. Jang, A. K. Nayak and H. Han, *Small Sci.*, 2024, **4**, 2300109.
43 Y. Zeng, Y. Wang, Q. Jin, Z. Pei, D. Luan, X. Zhang and X. W. Lou, *Angew. Chem., Int. Ed.*, 2021, **60**, 25793–25798.
44 J. Zhu, L. Xia, R. Yu, R. Lu, J. Li, R. He, Y. Wu, W. Zhang, X. Hong, W. Chen, Y. Zhao, L. Zhou, L. Mai and Z. Wang, *J. Am. Chem. Soc.*, 2022, **144**, 15529–15538.
45 T. Zhou, J. Bai, Y. Gao, L. Zhao, X. Jing and Y. Gong, *J. Colloid Interface Sci.*, 2022, **615**, 256–264.
46 Q. Liang, X. Yan, Z. Li, Z. Wu, H. Shi, H. Huang and Z. Kang, *J. Mater. Chem. A*, 2022, **10**, 4279–4287.
47 D. Wei, Y. Cao, L. Yan, H. Gang, B. Wu, B. Ouyang, P. Chen, Y. Jiang and H. Wang, *ACS Appl. Mater. Interfaces*, 2023, **15**, 24427–24436.
48 J. Feng, L. Qiao, P. Zhou, H. Bai, C. Liu, C. C. Leong, Y.-Y. Chen, W. F. Ip, J. Ni and H. Pan, *J. Mater. Chem. A*, 2023, **11**, 316–329.
49 T. Reier, Z. Pawolek, S. Cherevko, M. Bruns, T. Jones, D. Teschner, S. Selve, A. Bergmann, H. N. Nong, R. Schlögl, K. J. J. Mayrhofer and P. Strasser, *J. Am. Chem. Soc.*, 2015, **137**, 13031–13040.
50 V. Fung, F. F. Tao and D.-e. Jiang, *J. Phys. Chem. Lett.*, 2017, **8**, 2206–2211.
51 J. Shan, T. Ling, K. Davey, Y. Zheng and S.-Z. Qiao, *Adv. Mater.*, 2019, **31**, 1900510.
52 S. Niu, X.-P. Kong, S. Li, Y. Zhang, J. Wu, W. Zhao and P. Xu, *Appl. Catal., B*, 2021, **297**, 120442.
53 Q. Xia, Q. Zhang, S. Sun, F. Hussain, C. Zhang, X. Zhu, F. Meng, K. Liu, H. Geng, J. Xu, F. Zan, P. Wang, L. Gu and H. Xia, *Adv. Mater.*, 2021, **33**, 2003524.
54 K. Wang, Y. Wang, B. Yang, Z. Li, X. Qin, Q. Zhang, L. Lei, M. Qiu, G. Wu and Y. Hou, *Energy Environ. Sci.*, 2022, **15**, 2356–2365.

55 Z. Wu, Y. Wang, D. Liu, B. Zhou, P. Yang, R. Liu, W. Xiao, T. Ma, J. Wang and L. Wang, *Adv. Funct. Mater.*, 2023, **33**, 2307010.
56 M. P. Browne, H. Nolan, G. S. Duesberg, P. E. Colavita and M. E. G. Lyons, *ACS Catal.*, 2016, **6**, 2408–2415.
57 M. P. Browne, C. Domínguez, C. Kaplan, M. E. G. Lyons, E. Fonda and P. E. Colavita, *ACS Appl. Energy Mater.*, 2023, **6**, 8607–8615.
58 Z.-H. Yin, Y. Huang, K. Song, T.-T. Li, J.-Y. Cui, C. Meng, H. Zhang and J.-J. Wang, *J. Am. Chem. Soc.*, 2024, **146**, 6846–6855.
59 C. Liu, Z. Wei, M. Cao and R. Cao, *Nano Res.*, 2024, **17**, 4844–4849.
60 X. Zheng, J. Yang, P. Li, Q. Wang, J. Wu, E. Zhang, S. Chen, Z. Zhuang, W. Lai, S. Dou, W. Sun, D. Wang and Y. Li, *Sci. Adv.*, 2023, **9**, eadi8025.
61 M. Gollasch, J. Schmeling, C. Harms and M. Wark, *Adv. Mater. Interfaces*, 2023, **10**, 2300036.
62 Y. Zhao, J. Hu, C.-L. Chiang, Y. Li, W. Yang, Z. Yang, W.-H. Hung, Y.-G. Lin, Z. Chen, B. Li, P. Gao and H. Li, *J. Mater. Chem. A*, 2022, **10**, 20964–20974.
63 C. Lin, J.-L. Li, X. Li, S. Yang, W. Luo, Y. Zhang, S.-H. Kim, D.-H. Kim, S. S. Shinde, Y.-F. Li, Z.-P. Liu, Z. Jiang and J.-H. Lee, *Nat. Catal.*, 2021, **4**, 1012–1023.
64 S. Zhao, Y. Wang, J. Dong, C.-T. He, H. Yin, P. An, K. Zhao, X. Zhang, C. Gao, L. Zhang, J. Lv, J. Wang, J. Zhang, A. M. Khattak, N. A. Khan, Z. Wei, J. Zhang, S. Liu, H. Zhao and Z. Tang, *Nat. Energy*, 2016, **1**, 16184.
65 L.-Y. Chueh, C.-H. Kuo, R.-H. Yang, D.-H. Tsai, M.-H. Tsai, C.-C. Yang, H.-Y. Chen, C.-H. Wang and Y.-T. Pan, *Chem. Eng. J.*, 2023, **464**, 142613.
66 L. Chong, G. Gao, J. Wen, H. Li, H. Xu, Z. Green, J. D. Sugar, A. J. Kropf, W. Xu, X.-M. Lin, H. Xu, L.-W. Wang and D.-J. Liu, *Science*, 2023, **380**, 609–616.
67 Y. Li, X. Wei, S. Han, L. Chen and J. Shi, *Angew. Chem., Int. Ed.*, 2021, **60**, 21464–21472.
68 Y. Wen, P. Chen, L. Wang, S. Li, Z. Wang, J. Abed, X. Mao, Y. Min, C. T. Dinh, P. D. Luna, R. Huang, L. Zhang, L. Wang, L. Wang, R. J. Nielsen, H. Li, T. Zhuang, C. Ke, O. Voznyy, Y. Hu, Y. Li, W. A. Goddard Iii, B. Zhang, H. Peng and E. H. Sargent, *J. Am. Chem. Soc.*, 2021, **143**, 6482–6490.
69 S. Hao, M. Liu, J. Pan, X. Liu, X. Tan, N. Xu, Y. He, L. Lei and X. Zhang, *Nat. Commun.*, 2020, **11**, 5368.
70 M. T. M. Koper, *Chem. Sci.*, 2013, **4**, 2710–2723.
71 H. Jin, X. Liu, P. An, C. Tang, H. Yu, Q. Zhang, H.-J. Peng, L. Gu, Y. Zheng, T. Song, K. Davey, U. Paik, J. Dong and S.-Z. Qiao, *Nat. Commun.*, 2023, **14**, 354.
72 J. Wei, H. Tang, L. Sheng, R. Wang, M. Fan, J. Wan, Y. Wu, Z. Zhang, S. Zhou and J. Zeng, *Nat. Commun.*, 2024, **15**, 559.
73 B. You and S. Z. Qiao, *Chem.–Eur. J.*, 2021, **27**, 553–564.
74 R. Subbaraman, D. Tripkovic, K.-C. Chang, D. Strmcnik, A. P. Paulikas, P. Hirunsit, M. Chan, J. Greeley, V. Stamenkovic and N. M. Markovic, *Nat. Mater.*, 2012, **11**, 550–557.
75 M. Han, N. Wang, B. Zhang, Y. Xia, J. Li, J. Han, K. Yao, C. Gao, C. He, Y. Liu, Z. Wang, A. Seifitokaldani, X. Sun and H. Liang, *ACS Catal.*, 2020, **10**, 9725–9734.